Ceramics International 49 (2023) 22100–22109

Contents lists available at ScienceDirect

Ceramics International

journal homepage: www.elsevier.com/locate/ceramint

Design of novel photothermal conversion nanoparticles integrated with temperature self-response ability based on thermal-enhanced NIR to NIR luminescence

Guotao Xiang [a,*], Zhen Liu [a], Menglin Yang [a], Yongxi Ding [a], Lu Yao [a], Yongjie Wang [a], Xianju Zhou [a], Li Li [a], Li Ma [c], Xiaojun Wang [c,**], Jiahua Zhang [b,***]

[a] Department of Mathematics and Physics, Chongqing University of Posts and Telecommunications, 2 Chongwen Road, Chongqing, 400065, China
[b] State Key Laboratory of Luminescence and Applications, Changchun Institute of Optics, Fine Mechanics and Physics, Chinese Academy of Sciences, 3888 Eastern South Lake Road, Changchun, 130033, China
[c] Department of Physics & Astronomy, Georgia Southern University, Statesboro, GA, 30460, USA

ARTICLE INFO

Handling Editor: Dr P. Vincenzini

Keywords:
FIR thermometry
Fluorescence enhancement
Rare earth
Nanocrystals

ABSTRACT

The development of photothermal therapy (PTT) agents possessing temperature self-response ability and working in the deep tissues is an urgent need for noninvasive cancer treatment. Herein, a nanocomposite material hexagonal phase $NaLuF_4$: $Yb^{3+}/Nd^{3+}@SiO_2@Cu_2S$ is successfully constructed for the purpose of meeting the above demands. Under the irradiation of 980 nm near-infrared (NIR) light, the prepared nanocrystals (NCs) exhibit good photothermal conversion capacity and ultrasensitive temperature sensing properties along with remarkable resolution. The optical thermometry is realized by the fluorescence intensity ratio of Nd^{3+}: ^4F_j (j = 7/2, 5/2, and 3/2) levels, of which the NIR emission intensities are strongly enhanced with the increasing temperature due to the phonon-assisted energy transfer mechanisms between Yb^{3+} and Nd^{3+}. As the excitation and emission wavelength of the sample are all located in the biological window, its penetration depth in the biological tissues can be reached to 8 mm. The adsorptive Cu_2S NCs on the surface of $NaLuF_4$: $Yb^{3+}/Nd^{3+}@SiO_2$ provide the required light-to-heat conversion capacity, which has been investigated in detail through the laser-irradiated and bactericidal experiment respectively. These findings provide a feasible strategy to design high-performance PTT agents integrated with precise temperature self-measurement function for deep-tissue therapy.

1. Introduction

Nowadays, the emerging concept of noninvasive treatment makes photothermal therapy (PTT) become a hopeful strategy for cancer therapy thanks to its advantages of minimal invasiveness, few side effects, high selectivity, etc. Up to now, a large number of inorganic nanomaterials with efficient photothermal conversion performance has been utilized as the PTT agents (PTAs), such as metal nanocrystals (NCs), metal chalcogenides, semiconductors, carbon materials and so on [1–4]. Among the numerous numbers of PTAs, copper chalcogenide (Cu_xS) NCs are regarded as the ideal candidates for PTT process due to the strong absorption and heat conversion ability for near-infrared (NIR) light along with environment-friendly synthetic method, excellent stability and low toxicity [5–7].

Unfortunately, the absence of accurate method for temperature monitoring during the PTT process often causes ineffective treatment to the pathological cells by lack of heat or undesirable damage to the normal tissues by the overheating effect [8]. Fluorescence intensity ratio (*FIR*) thermometry based on the thermal coupled levels (TCLs) of rare earth ions is proposed to be an ideal method to settle the above matter, which can be assembled with PTAs to realize a self-monitored PTT process [9–12]. The green emitting levels of Er^{3+}: $^4S_{3/2}/^2H_{11/2}$ with the energy gap (ΔE) of approximately 800 cm^{-1} are the most widely studied TCLs for temperature sensing. However, the shallow penetration depth and modest sensitivity severely restrict their availability for biological applications [13,14]. The thermometric sensitivity of rare earth

* Corresponding author.
** Corresponding author.
*** Corresponding author.
E-mail addresses: xianggt@cqupt.edu.cn (G. Xiang), xwang@georgiasouthern.edu (X. Wang), zhangjh@ciomp.ac.cn (J. Zhang).

https://doi.org/10.1016/j.ceramint.2023.04.037
Received 26 February 2023; Received in revised form 1 April 2023; Accepted 6 April 2023
Available online 6 April 2023

ions-based optical thermometers can be intensely elevated by using the TCLs with large ΔE, such as Nd^{3+}: $^4F_{7/2}/^4F_{3/2}$ (~1900 cm^{-1}). Compared with other TCLs with considerable ΔE, such as Tm^{3+}: $^3F_{2,3}/^3H_4$ (~1700 cm^{-1}) and Eu^{3+}: $^5D_0/^5D_1$ (~1750 cm^{-1}), the existence of intermediate level Nd^{3+}: $^4F_{5/2}$ between $^4F_{7/2}$ and $^4F_{3/2}$ level can effectively avoid the occurrence of decoupling effect in the low temperature range [15–18]. Meanwhile, the penetration depth can be expected to be improved by employing Nd^{3+}: $^4F_{7/2}/^4F_{3/2}$ as the thermometric cursors under the sensitization of Yb^{3+} ions (excited by 980 nm), resulting from that the excitation and emission positions in Yb^{3+}/Nd^{3+} codoped NCs all locate in the biological window (650 nm–1000 nm). In addition, the luminescence quenching caused by the increasing temperature can also be drastically suppressed in Yb^{3+}/Nd^{3+} codoped system due to the fact of phonon-assisted (PA) energy transfer (ET) mechanisms between them [19–23]. Therefore, it is a reasonable prospect that a high-performance PTT with the function of precise temperature self-measurement can be realized in the deep tissues through integrating excellent PTAs with Yb^{3+}/Nd^{3+} codoped NCs.

In this paper, a new-type nanostructure of hexagonal phase (β) $NaLuF_4$: $Yb^{3+}/Nd^{3+}@SiO_2@Cu_2S$ is successfully fabricated by the wet chemistry method, in which an excellent temperature sensing property based on the thermal-enhanced NIR to NIR luminescence and remarkable photothermal conversion performance based on the Cu_2S NCs are simultaneously realized under the excitation of 980 nm wavelength. Beyond that, the penetration depth and the photothermal conversion ability of the present NCs are evaluated by the designed *ex vivo* experiments.

2. Experimental

2.1. Chemicals

$LuCl_3$, $NdCl_3$ and $YbCl_3$ (99.99%) are supplied by Beijing Founde Star Science & Technology Co, Ltd. Cyclohexane, methanol, acetone, hydrochloric acid, ethanol, NH_4F, NH_4OH (30 wt%), $CuCl_2{\cdot}2H_2O$, $Na_2S{\cdot}9H_2O$, $Na_3C_6H_5O_7{\cdot}2H_2O$ and NaOH are obtained from Chongqing Chuandong Chemical (Croup) Co, Ltd. 1-octadecene (ODE, 90%) and Oleic acid (OA, 90%) are acquired from Alfa Aesar. CO-520, tetraethoxysliane (TEOS) and aminopropyltrimethoxysliane (APTMS) are supplied by Aladdin. Phosphate buffered saline (PBS), agar medium and nutrient broth are purchased from Beijing Land Bridge Technology Co, Ltd. Escherichia coli (ATCC25922) is obtained from Shanghai Luwei Technology Co, Ltd. All the reagents are used for the present experiments directly without any purification.

2.2. Synthesis of β-$NaLuF_4$: x%Yb^{3+}/y% Nd^{3+} (NLYN) NCs (x = 0, 1, 5, 10, 20, 30, 40; y = 1, 2, 3)

In a typical preparation procedure, rare earth chlorides are weighed in an appropriate proportions according to nominal composition β-$NaLuF_4$: x%Yb^{3+}/y% Nd^{3+} NCs (x = 0, 1, 5, 10, 20, 30, 40; y = 1, 2, 3) and then transferred them into a 100 ml three-necked flask containing 12 ml OA and 28 ml ODE. In the nitrogen gas atmosphere, the solution is first heated to 140 °C and maintained for 30 min to dissolve the solid powder thoroughly. After that, 10 ml methanol mixed with 3.2 mmol NH_4F and 0.8 mmol NaOH are injected into the reaction solution when its temperature is cooled down to 70 °C. This status is kept for 30 min to completely evaporate the methanol. Subsequently, the reactant complex is raised to 300 °C, kept for 1.5 h and then cooled to room temperature naturally to form the product NLYN NCs. Finally, the resulting solution is precipitated by adding ethanol, centrifuged and cleaned with a mixture of alcohol and tertiary water.

2.3. Synthesis of NLYN@SiO_2 NCs

Firstly, the prepared NLYN NCs are dispersed in 10 ml cyclohexane and 0.1 ml CO-520 along with stirring for 10 min. After that, 0.08 ml ammonium hydroxide and another 0.4 ml CO-520 are poured into the above solution accompanied by a 20 min' ultrasound process under sealed condition. After the formation of a transparent emulsion, 0.04 ml TEOS is added to the mixture followed by continuous stirring procedure for 12 h. Finally, the NLYN@SiO_2 NCs is precipitated by adding excess acetone and washed with tertiary water and ethanol.

2.4. Synthesis of NLYN@SiO_2@Cu_2S NCs

Firstly, 100 ml aqueous solution A containing 2 ml of $Na_2S{\cdot}9H_2O$ (0.04 M), 0.014 g $CuCl_2{\cdot}2H_2O$ and 0.02 g $Na_3C_6H_5O_7{\cdot}2H_2O$ is heated to 90 °C for 20 min accompanied by continuous stirring until the formation of Cu_2S NCs with dark green color, which should be reserved in 4 °C ice water for subsequent preparation procedure. Secondly, 0.15 ml APTMS is added dropwise into 50 ml ethanol solution containing 0.1 g NLYN@SiO_2 NCs under stirring condition for 12 h to form solution B. After that, 40 ml solution A is mixed with the above solution B along with a 2 h' stirring process to generate the target product. Finally, the NLYN@SiO_2@Cu_2S NCs are collected by centrifugation and cleaned by water and ethanol for several times.

2.5. Bactericidal experiment based on photothermal conversion

E. coli is firstly placed in a sterile nutrient solution diluted with sterile water and then equal amounts of bacterial solution are transferred to four flasks. On the one hand, 100 μL PBS buffer solution without NCs are added in the first two flasks, marked as Control group and NIR group respectively. On the other hand, the remaining two flasks are all mixed with 100 μL PBS buffer solution containing NLYN@SiO_2@Cu_2S NCs (1 mg mL^{-1}), named NCs group and NCs + NIR group respectively. After that, the four bacterial groups are migrated to their corresponding agar mediums. Moreover, the 980 nm NIR light with a power density of 12 mW/mm^2 is utilized to irradiate the NIR group and NCs + NIR group for 15 min. Finally, the four bacterial groups are all cultivated at 37 °C for 24 h in the air and then taken out to observe the bacterial amount of each group.

2.6. Characterization

An XD-2 diffractometer produced by Beijing Persee is utilized to collect the powder X-ray diffraction (XDR) data. The morphology and element analysis data are acquired by a JEOL JEM 2100 transmission electron microscope (TEM) equipped with an energy-dispersive X-ray spectrometer (EDS). A Cary 5000 UV–vis–NIR spectrophotometer is employed to measure the absorption spectra. The spectroscopic data is detected by a FLS1000 spectrometer equipped with a 980 nm laser as the excitation source. The sample temperature during the spectral measurement process is controlled by a HFS600E-PB2 temperature control device supplied by Scientific Instruments. The photothermal conversion effect is monitored by a Digi-Sense thermocouple thermometer with a minimum resolution of 0.1 *K*.

3. Results and discussion

3.1. Structure and morphology

The XRD patterns of the NLYN NCs doped with various Yb^{3+} and Nd^{3+} concentrations are shown in Fig. 1 (a) and (b). Notably, the positions and relative intensity of the diffraction peaks are well indexed to the standard cards of hexagonal phase $NaLuF_4$ (JCPDS No. 27-0726). No impure phase is found except the residual NaCl, which is marked by an asterisk, exhibiting that the Yb^{3+} and Nd^{3+} ions are all inserted into the β-$NaLuF_4$ matrix to form a so-called solid solution structure. In addition, the diffraction peaks slightly shift to the low angle direction due to the substitution of Lu^{3+} (0.85 Å) ions by Yb^{3+} (0.86 Å) and Nd^{3+} (1.00 Å)

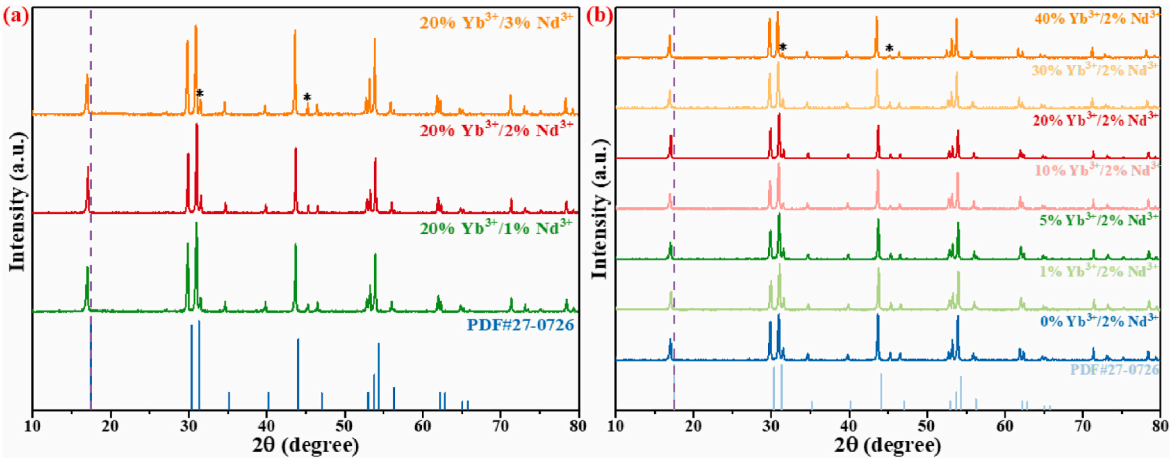

Fig. 1. The XRD patterns of (a) β-$NaLuF_4$: 20% Yb^{3+}/y% Nd^{3+} and (b) β-$NaLuF_4$: x% Yb^{3+}/2% Nd^{3+} NCs.

ions with larger radius.

Subsequently, the obtained NLYN NCs are coated by SiO_2 shell and then adsorbed by small Cu_2S NCs. The corresponding XRD patterns of the prepared samples are displayed in Fig. 2(a), from which it can be clearly seen that the NCs synthesized at each step are all matched well with the standard cards of β-$NaLuF_4$ (JCPDS No. 27-0726), resulting from the tiny amount of SiO_2 and Cu_2S existing in the samples. Fig. 2(b) illustrates the detailed preparation process of NLYN@SiO_2@Cu_2S NCs. The first step is to epitaxially grow a SiO_2 shell on the surface of NLYN NCs utilizing TEOS as the raw material for the purpose of hydrophilia. Next, the above NCs are modified by APTMS and then combined with small Cu_2S NCs by force of electrostatic adsorption.

The TEM technology is used to describe the morphology and size evolution of the samples caused by Yb^{3+} and Nd^{3+} doping, as shown in Fig. 3(a)-(h). Obviously, the morphology of the NCs is almost unchanged with the variation of Yb^{3+} and Nd^{3+} ions concentration, displaying uniform hexagonal nanoplate with a diameter of about 440 nm. After the epitaxial growth of SiO_2, the size of NCs is increased to approximately 460 nm without any significant change in morphology, which means that the SiO_2 layer with 10 nm thickness has been built on the surface of NLYN NCs, as shown in Fig. 3(i). Meanwhile, the EDS line profiles of NLYN@SiO_2 are also measured to further demonstrate the successful coating of SiO_2 shell. As can be seen from Fig. 3(k), the elements of Na, Lu, F, Yb and Nd are homogenously distributed in the interior of the NCs, but the Si and O element are mainly found at the outer surface of the particles. Fig. 3(j) shows the TEM image of a single NLYN@SiO_2@Cu_2S nanoparticle, which is fabricated by virtue of electrostatic adhesion effect between APTMS-modified NLYN@SiO_2 NCs with positive charge and small Cu_2S NCs with negative charge. The well-resolved lattice fringes detected by high-resolution TEM (HR-TEM) show an interplanar spacing of 2.82 Å in the inner of NCs and 2.01 Å in the attached small NCs, corresponding to (101) crystal plane of β-$NaLuF_4$ (JCPDS No. 27-0726) and (110) crystal plane of Cu_2S (JCPDS No. 26-1116) respectively, as presented in Fig. 3(l). In addition, elemental mapping images are captured in Fig. 3(m) to explore the elemental composition of the prepared samples, in which Na, Lu, F, Yb, Nd, Si, O, Cu and S are all emerged in a single nanoparticle, once again demonstrating the successful construction of NLYN@SiO_2@Cu_2S NCs.

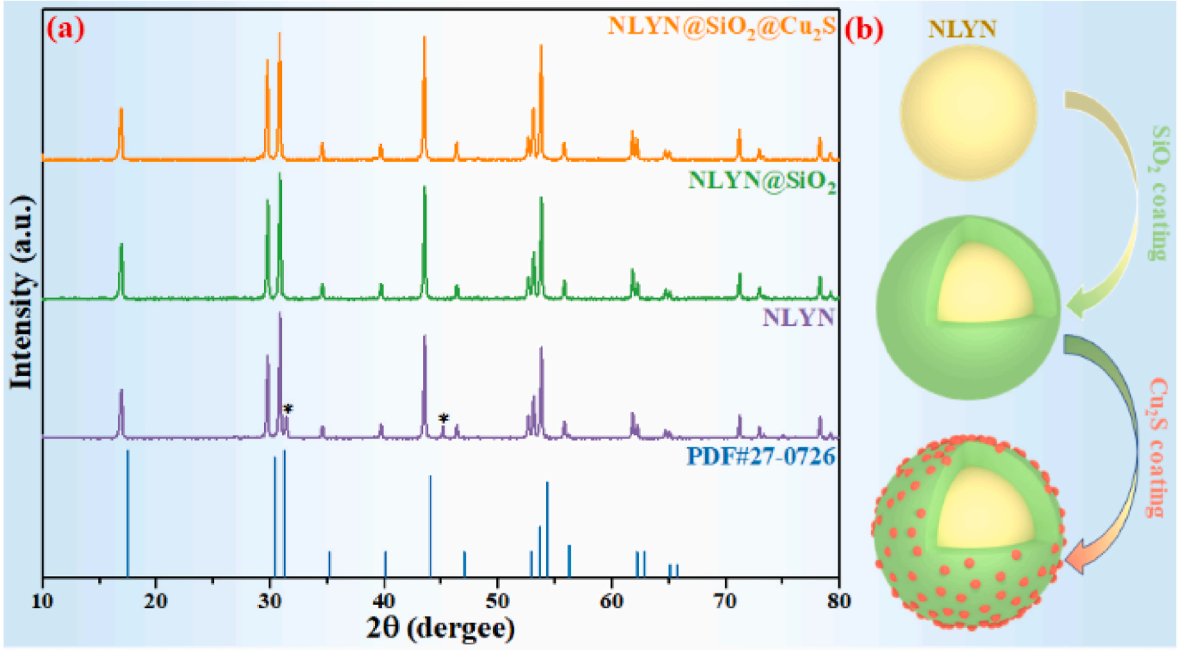

Fig. 2. (a) XRD diffraction patterns of NLYN, NLYN@SiO_2 and NLYN@SiO_2@Cu_2S. (b) The flowchart for the preparation of NLYN@SiO_2@Cu_2S NCs.

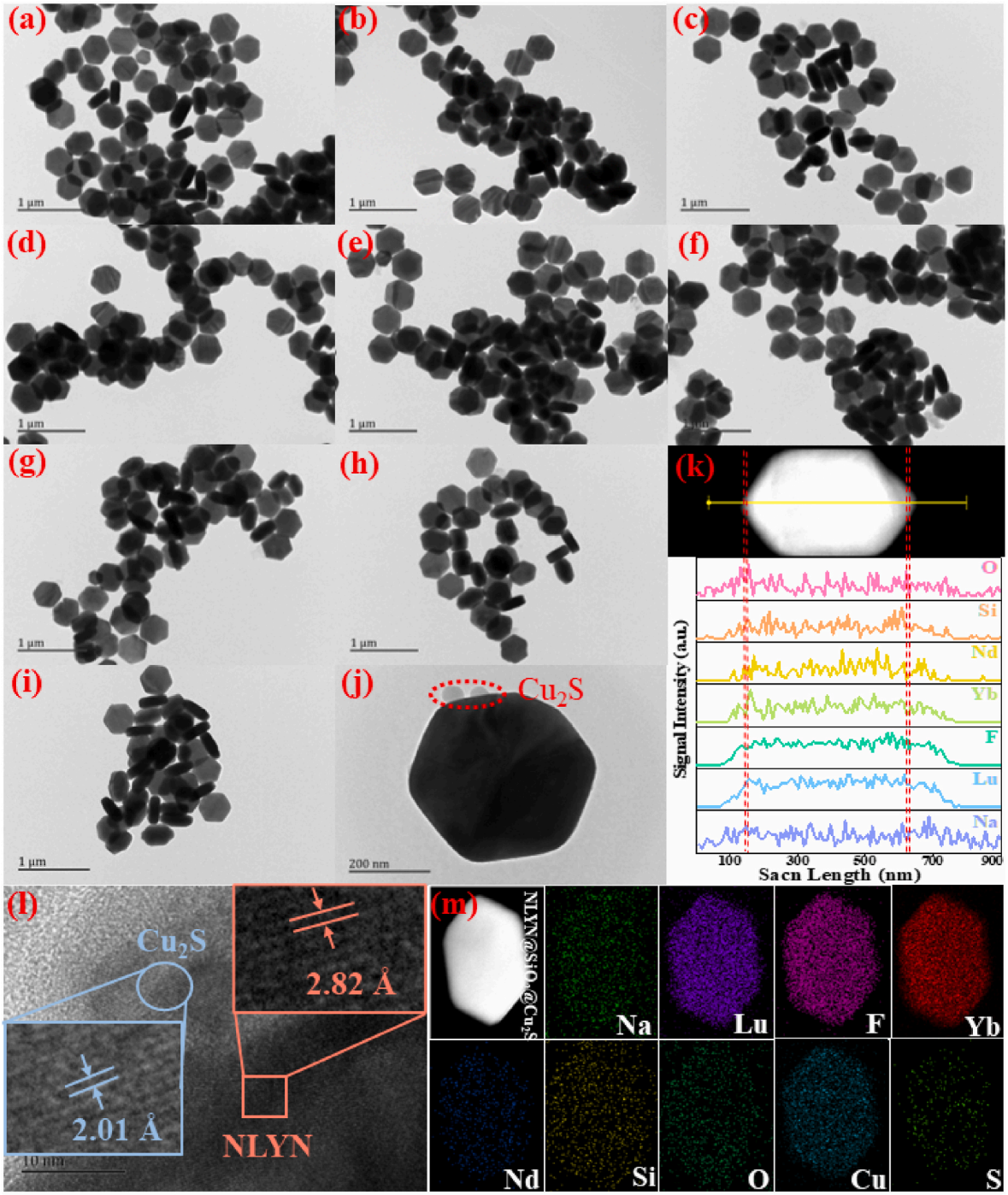

Fig. 3. TEM images of NLYN NCs doped with (a)–(c) 10% Yb^{3+}/y% Nd^{3+} (y = 1, 2, 3) and (d)–(h) x% Yb^{3+}/2% Nd^{3+} (x = 0, 1, 5, 20, 30). TEM images of (i) NLYN@SiO_2 and (j) NLYN@SiO_2@Cu_2S. (k) EDS line scan of NLYN@SiO_2. (l) HR-TEM image of NLYN@SiO_2@Cu_2S. (m) Element mapping images of NLYN@SiO_2@Cu_2S.

3.2. Luminescence properties

Fig. 4(a) and (b) display the emission spectra of the unmodified samples under the excitation of 980 nm wavelength. Obviously, three emission bands appear in the NIR region of 700 nm–900 nm, which belongs to Nd^{3+}: $^4F_{7/2} \rightarrow {}^4I_{9/2}$ at 741 nm, Nd^{3+}: $^4F_{5/2} \rightarrow {}^4I_{9/2}$ at 794 nm and Nd^{3+}: $^4F_{3/2} \rightarrow {}^4I_{9/2}$ at 864 nm. The overall emission intensity of the samples doped with a fixed Yb^{3+} concentration is first enhanced and then weakened with the increasing Nd^{3+} concentration because of the concentration quenching effect, by which the optimal doping concentration of Nd^{3+} can be determined to be 2%. Similarly, the optimal doping concentration of Yb^{3+} is ascertained to be 10%, as shown in Fig. 4(b). That is to say, the strongest emission intensity is obtained in the NCs doped with 10% Yb^{3+} ion and 2% Nd^{3+} ion, which will be used as the study subject in the following discussion. In addition, the variation of Yb^{3+} and Nd^{3+} doping concentration has no influence on the position of the NIR emission peaks.

Sequentially, the 10% Yb^{3+} and 2% Nd^{3+} codoped NCs are utilized to synthesize the NLYN@SiO_2 and NLYN@SiO_2@Cu_2S. The photoluminescence (PL) spectra of the above NCs excited by 980 nm wavelength are measured and depicted in Fig. 5(a). Distinctly, the PL intensity of NLYN NCs is enhanced by a factor of 1.9 after coating a SiO_2

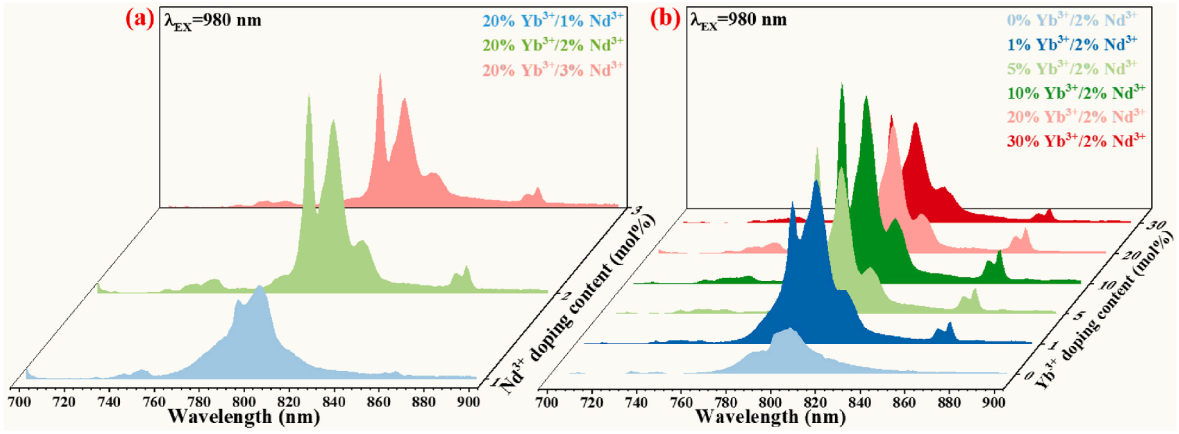

Fig. 4. Emission spectra of NLYN NCs doped with (a) 20% Yb^{3+}/y% Nd^{3+} (y = 1, 2, 3) and (b) x% Yb^{3+}/2% Nd^{3+} (x = 0, 1, 5, 10, 20, 30).

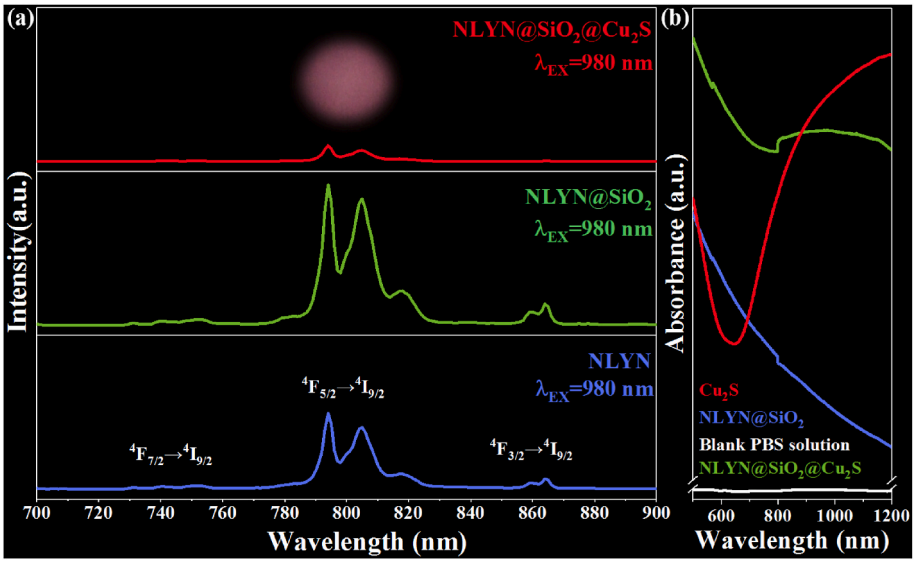

Fig. 5. (a) Emission spectra of NLYN, NLYN@SiO_2 and NLYN@SiO_2@Cu_2S. (b) Absorption spectra of NLYN@SiO_2, NLYN@SiO_2@Cu_2S and Cu_2S NCs dispersed in PBS solution as well as blank PBS solution. The inset in (a) is the digital photo of NLYN@SiO_2@Cu_2S excited by 980 nm wavelength.

shell, which is ascribed to the improvement of light extraction efficiency from the inside of NCs to the ambience. Specifically, the light travelling from an optically denser medium (refractive index named n_{r2}) to an optically thinner medium (refractive index named n_{r1}) should be totally reflected at the interface when its incidence angle (θ) is larger than a critical value ($\theta_C = \arcsin(n_{r1}/n_{r2})$), which is the so-called total internal reflection (TIR) phenomenon. In the bare NLYN NCs ($n \approx 1.52$), the value of critical angle θ_{C0} for the light travelling from the inside of the NLYN NCs to the air ($n = 1$) is calculated to be about 41° [24]. After introducing a SiO_2 ($n \approx 1.46$) shell between the NLYN NCs and air, the corresponding value is increased to be 74° at the interface of the NLYN and SiO_2 and 43° at the interface of SiO_2 and air, which means that more light is allowed to escape the NCs through SiO_2 layer modification [25]. Beyond that, the SiO_2 shell can also reduce the ET processes from the luminescence centers to surface defects, resulting in the PL enhancement. However, the emission intensity of the sample is dramatically decreased due to the decoration of small Cu_2S NCs. As shown in Fig. 5 (b), the NLYN@SiO_2@Cu_2S NCs exhibit much stronger absorption for red and NIR light than NLYN@SiO_2 NCs benefitting from the outstanding absorptive capacity of Cu_2S NCs in the region from 600 nm to 1200 nm, in which the emission bands of Nd^{3+} ions are included. Hence, the efficient absorption of Cu_2S for the excitation light produced by 980 nm semiconductor laser and emission light originated from the Nd^{3+} ions gives rise to the decrease of the whole emission intensity of the NCs. Even then, the intense emission of Nd^{3+} ions in NLYN@SiO_2@Cu_2S NCs can also be detected under 980 nm excitation, as visualized in the inset of Fig. 5(a), which belongs to the far-red luminescence of Nd^{3+}: $^4F_{7/2} \rightarrow {}^4I_{9/2}$ transition.

For application in biological tissues, penetration depth is a vital value to assess the practicality of the optical probes. Therefore, the NIR emission assigned to Nd^{3+}: ^4F_j (j = 7/2, 5/2, and 3/2) → $^4I_{9/2}$ transition in NLYN@SiO_2@Cu_2S NCs are collected with various biological tissue thickness at room temperature. Evidently, as depicted in Fig. 6(a), the NIR luminescence intensity of the NCs is gradually decreased with the thickened chicken tissues, but no obvious change is found on spectral profile. Nevertheless, the spectral information of the sample can still be acquired at a depth of 8 mm, revealing the great potential of NLYN@SiO_2@Cu_2S NCs for utilization in deep tissues, which benefits from the excitation and emission wavelength of the NCs locating in the biological window.

As illustrated in Fig. 6(b), the NIR to NIR emission of Nd^{3+} ions sensitized by Yb^{3+} ions results from two possible PA ET pathways, including a single-phonon process (ET1) and a two-phonon process (ET2 and ET3). In the single-photon process (ET1), excited Yb^{3+} ion transfers its energy to the nearby Nd^{3+} ion in the ground state via the PA ET1 process, resulting in the population of Nd^{3+}: $^4F_{3/2}$ state. In the two-

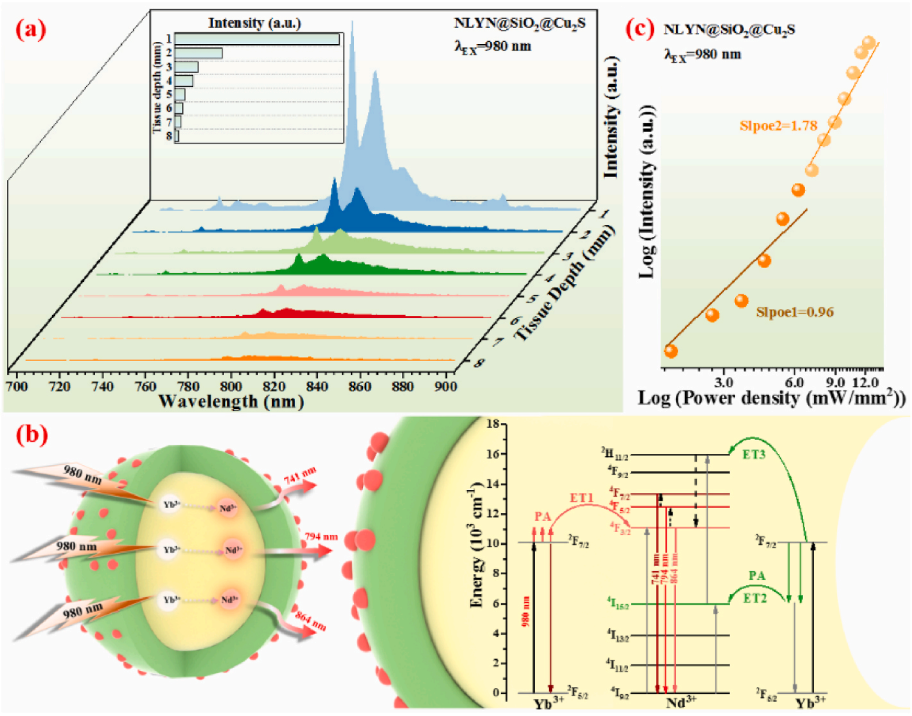

Fig. 6. (a) Emission spectra of NLYN@SiO_2@Cu_2S NCs with various biological tissue thickness. (b) Possible ET mechanisms in NLYN@SiO_2@Cu_2S NCs. (c) Log(*I*) - log(*P*) diagram of Nd^{3+}: $^4F_{5/2} \rightarrow {}^4I_{9/2}$ transition in NLYN@SiO_2@Cu_2S NCs.

photon process, the Nd^{3+} ion locating in the ground state is firstly populated to its $^4I_{15/2}$ level by gaining energy from the Yb^{3+} ion at the excited level with the assistance of phonon vibrations (ET2). Sequentially, this Nd^{3+} ion can be populated to $^4F_{3/2}$ state through another ET process between Yb^{3+} and Nd^{3+} (ET3) followed by a non-radiative (NR) process from Nd^{3+}: $^2H_{11/2}$ level, during which the excess energy is converted into heat. The Nd^{3+} at $^4F_{3/2}$ state can be further excited to $^4F_{5/2}$ and $^4F_{7/2}$ level with the aid of active lattice phonons, benefiting from their small ΔE value.

The power density dependence of the emission intensity in NLYN@SiO_2@Cu_2S NCs is exhibited in Fig. 6(c) to qualitatively analyze the ET mechanisms in Yb^{3+} and Nd^{3+} co-doped system. The relationship between emission intensity (*I*) and power density (*P*) can be written as follows:

$$I \propto P^n \quad (1)$$

Here, *n* is the NIR photon number that needs to be absorbed for emitting a high-energy photon, which can be obtained by the slope of the linear curve of log(*I*) - log(*P*) [26,27]. Evidently, the *n* value of Nd^{3+}: $^4F_{5/2} \rightarrow {}^4I_{9/2}$ transition changes from 0.96 to 1.78 as the excitation power density surpasses 6.23 mW/mm^2, indicating that the single-photon ET processes are dominant at low power density, and the two-photon ET processes appear and gradually increase with the rising excitation power density. Similar situations are also found in NLYN and NLYN@SiO_2 NCs, as shown in Fig. S1.

3.3. Optical thermometry

As discussed in the preceding section, lattice phonon is regarded as the important role for the realization of Nd^{3+}: ^4F_j (j = 7/2, 5/2, 3/2) $\rightarrow {}^4I_{9/2}$ transition in Yb^{3+}/Nd^{3+} co-doped system, which is intensively

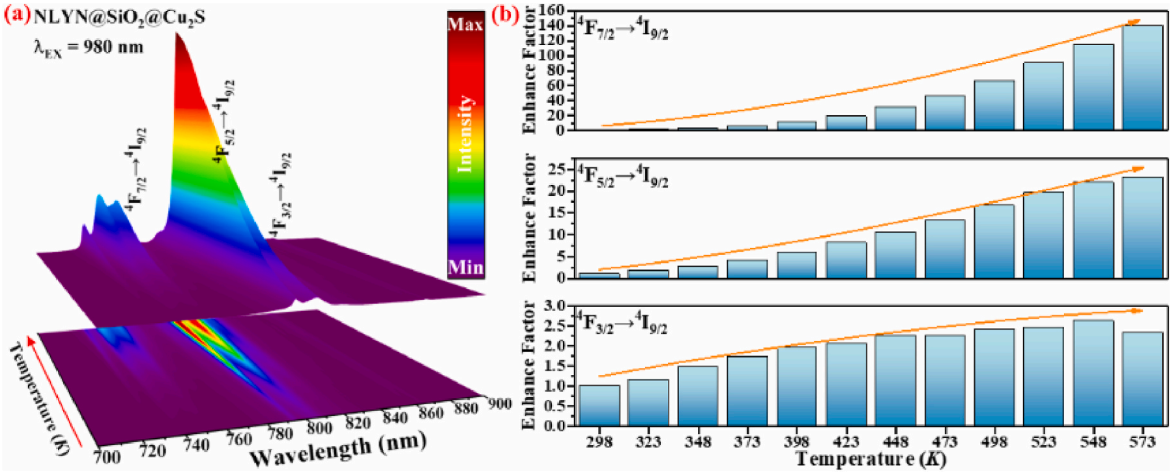

Fig. 7. (a) Temperature-dependent NIR spectra of NLYN@SiO_2@Cu_2S NCs in the range of 298–573 *K*. (b) Enhance factor of Nd^{3+}: ^4F_j (j = 7/2, 5/2, 3/2) $\rightarrow {}^4I_{9/2}$ transition at different temperature.

influenced by the ambient temperature. Thereby, the temperature dependence of Nd^{3+}: ^4F_j (j = 7/2, 5/2, 3/2) → $^4I_{9/2}$ transition in NLYN@SiO_2@Cu_2S NCs is measured under the excitation of 980 nm wavelength. As shown in Fig. 7(a), remarkable enhancement of NIR luminescence derived from Nd^{3+}: ^4F_j (j = 7/2, 5/2, 3/2) → $^4I_{9/2}$ transition is discovered through increasing the temperature from 298 *K* to 573 *K*. Especially, the emission intensity of Nd^{3+}: $^4F_{7/2}$ → $^4I_{9/2}$ transition shows a 160-fold improvement from 298 *K* to 573 *K*, as displayed in Fig. 7(b). Such a supernormal enhancement is attributed in part to the efficiency improvement of PA ET processes from Yb^{3+} to Nd^{3+} at high temperature. Beyond that, thermal coupling population from the low energy state $^4F_{3/2}$ and $^4F_{5/2}$ to high energy state $^4F_{7/2}$ are also dramatically intensified with the rising temperature, resulting in the same order of thermal-enhanced factors and their corresponding energy level positions. In addition, the thermal-enhanced luminescence properties in NLYN and NLYN@SiO_2 NCs are also investigated under 980 nm excitation, which are similar as that in NLYN@SiO_2@Cu_2S NCs, as shown in Fig. S2 and Fig. S3.

Considering the thermal coupling properties of Nd^{3+}: ^4F_j (j = 7/2, 5/2, 3/2), temperature sensing behaviors can be realized in NLYN@SiO_2@Cu_2S NCs based on fluorescence intensity ratio (*FIR*) technology. Fig. 8(a) shows the normalized PL spectra of Nd^{3+}: ^4F_j (j = 7/2, 5/2, 3/2) → $^4I_{9/2}$ transition driven by 980 nm wavelength, from which regular variation of relative intensities can be observed with the elevating temperature. Actually, the *FIR* value between two TCLs can be expressed as:

$$FIR = I_2/I_1 = (\omega_2 A_2 g_2/\omega_1 A_1 g_1)\cdot\exp(-\Delta E/kT) = B\cdot\exp(-\Delta E/kT), \quad (2)$$

where ω, A, g, I, k and T represent the angular frequency, spontaneous emission rate, degeneracy, emission intensity, Boltzmann's constant and absolute temperature respectively, B is defined as $\omega_2 A_2 g_2/\omega_1 A_1 g_1$ [28–31]. Utilizing equation (2), the *FIR* fitting curves of NLYN@SiO_2@Cu_2S NCs are calculated and shown in Fig. 8(b), from which the ΔE values are obtained to be 965 cm^{-1}, 1042 cm^{-1} and 2125 cm^{-1}, corresponding to $^4F_{7/2}$/$^4F_{5/2}$ (TCL1), $^4F_{5/2}$/$^4F_{3/2}$ (TCL2) and $^4F_{7/2}$/$^4F_{3/2}$ (TCL3). The above ΔE values obtained from the fitting curves are closed to those gained by the PL spectra with relative errors of about 6.6% (TCL1), 2.1% (TCL2) and 9.6% (TCL3) respectively. Meanwhile, the two major parameters, absolute sensitivity S_A and relative sensitivity S_R, can be calculated by the following equations to make a quantitative evaluation for the optical thermometers:

$$S_A = |d(FIR)/dT| = FIR\cdot\Delta E/(K_B\cdot T^2), \quad (3)$$

$$S_R = |d(FIR)/(FIR)\cdot dT| = \Delta E/(K_B\cdot T^2). \quad (4)$$

As depicted in Fig. 8(c) and (d), the S_A curves of TCL1, TCL2 and TCL3 go up with the rising temperature and reach their corresponding maximum values of 0.11% K^{-1}, 37.8% K^{-1} and 19.6% K^{-1} at 573 *K*, but their S_R curves show a downtrend when the temperature increases from 298 *K* to 573 *K*. Of these, TCL2 owns the highest S_A value due to the large *FIR* between $^4F_{5/2}$ and $^4F_{3/2}$ level, and TCL3 exhibits the best performance in S_R benefitting from the considerable ΔE between $^4F_{7/2}$ and $^4F_{3/2}$ level. Next, a confirmatory experiment is conducted to estimate the thermometry accuracy of TCL1, TCL2 and TCL3, in which an electrical heat gun is used to heat the sample, and both *FIR* technique and infrared thermometer are employed to detect the sample temperature. As shown in Fig. S4, the sample temperature is almost linearly raised under the heating action of heat gun. Moreover, the temperature measured by *FIR* technique matches well with the actual value determined by the infrared thermometer, especially FIR_{TCL2} and FIR_{TCL3}, manifesting the outstanding thermometry properties of NLYN@SiO_2@Cu_2S NCs. The small temperature deviation between the actual and measured values should be ascribed to the heat loss during the spectra collection process. The repeatability studies of TCL1, TCL2 and TCL3 in the temperature cycling between 298 *K* and 573 *K* are also measured and shown in Fig. S5. All of them keep almost unchanged after conducting six cycling process, revealing the excellent repeatability of NLYN@SiO_2@Cu_2S NCs for temperature measurement. In addition, as presented in Figs. S6 and S7, the temperature sensing properties of NLYN and NLYN@SiO_2 NCs are also investigated in detail, of which the corresponding S_R curve is similar as that of NLYN@SiO_2@Cu_2S NCs, resulting from the uselessness of SiO_2 coating and Cu_2S adhesion on changing energy separation between TCLs. However, the S_A values of TCL1, TCL2 and TCL3 in NLYN@SiO_2@Cu_2S NCs show a slight increase after SiO_2 and Cu_2S modification, which may be caused by the 10 nm SiO_2 layer and the gradually improving light absorption capacity of Cu_2S NCs in the region from 700 nm to 900 nm. The thermometric parameters of NLYN, NLYN@SiO_2 and NLYN@SiO_2@Cu_2S NCs are listed in Table S1.

Another important parameter for optical thermometers is

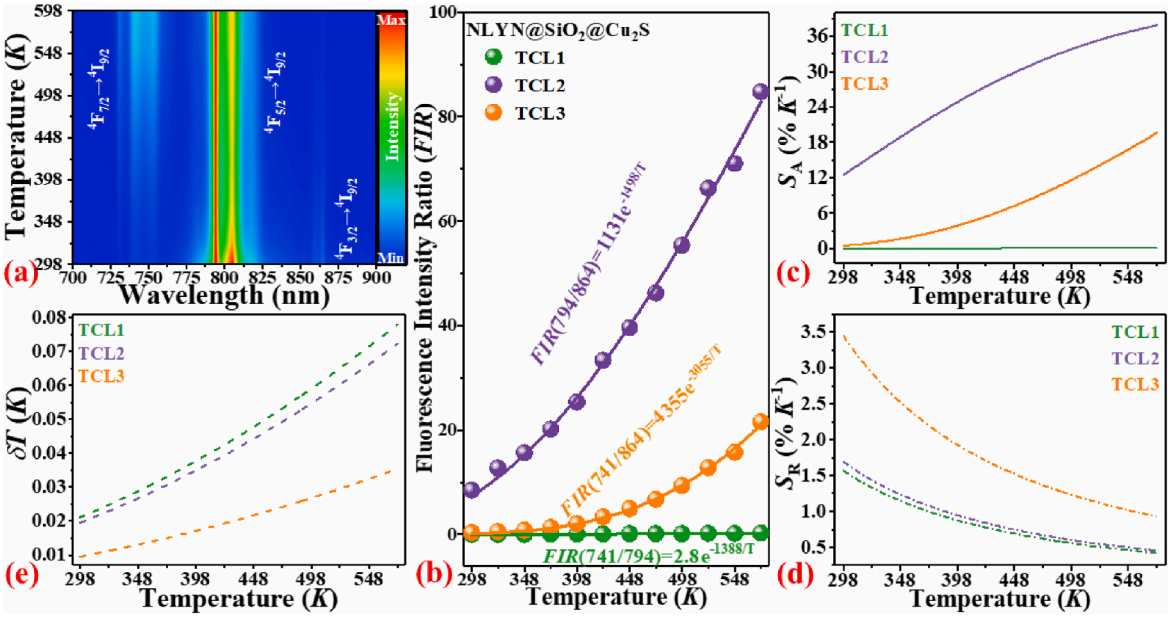

Fig. 8. (a) Temperature-dependent normalized PL spectra of NLYN@SiO_2@Cu_2S NCs. The (b) *FIR*, (c) absolution sensitivity S_A, (d) relative sensitivity S_R and (e) temperature resolution δT as a function of temperature in NLYN@SiO_2@Cu_2S NCs.

temperature resolution δT, which is expressed by the following equation:

$$\delta T = (\delta FIR/FIR)\cdot(1/S_R). \quad (5)$$

Here, $\delta FIR/FIR$ denotes the relative uncertainty of *FIR*, related to the equipment for spectral measurement [32]. Therefore, 50 times' repeated measurement for PL spectra are completed at 298 *K* and the $\delta FIR/FIR$ value is determined to be approximately 0.033% in our case (see Fig. S8). Based on the achieved $\delta FIR/FIR$ value, the optimal δT of TCL1, TCL2 and TCL3 is calculated to be 0.021, 0.019 and 0.009 *K* respectively at the beginning temperature, and then the δT curves are increased with the rising temperature, as shown in Fig. 8(e). Even so, the δT value of NLYN@SiO_2@Cu_2S NCs is consistently no more than 0.08 *K* within the entire range of the testing temperature, which is well enough to meet the requirement of biological application [33].

In order to perform an overall comparison with other typical Nd^{3+}-based optical thermometers reported previously, a detailed statistic involving operating temperature range and sensitivity is conducted in Table 1. Strikingly, NLYN@SiO_2@Cu_2S NCs possess the largest S_A and S_R values among the various Nd^{3+}-based optical thermometers. Particularly, the S_A value of the present NCs (37.8% K^{-1}) is 2 times higher than the reported highest value obtained in $LaPO_4$: Yb^{3+}/Nd^{3+} NCs (18.53% K^{-1}). Moreover, the NLYN@SiO_2@Cu_2S NCs also display outstanding thermometric sensitivity in comparison with Er^{3+}-based optical thermometers, which attract the most extensive attention for optical temperature sensing over the past decades. Until now, the reported optimal S_A and S_R in Er^{3+}-based temperature sensors realized by the TCLs $^2H_{11/2}/^4S_{3/2}$ is 2.3% K^{-1} in $NaLa(MoO_4)_2$: Yb^{3+}/Er^{3+} and 1.68% K^{-1} in $NaYF_4$: Yb^{3+}/Er^{3+} respectively, far from the values obtained in NLYN@SiO_2@Cu_2S NCs ($S_{A\text{-}Max} = 37.8\%\ K^{-1}$ and $S_{R\text{-}Max} = 3.45\%\ K^{-1}$ in our case) [37,38]. Beyond that, the prepared sample shows superior performance on δT (below 0.08 *K*, $\delta T_{min} = 0.009$ *K*) compared with previous reports, such as $NaYF_4$: Yb^{3+}/Er^{3+} (~0.1 *K*), Bi_2SiO_5: Yb^{3+}/Tm^{3+}@SiO_2 (~0.28 *K*), $[Gd_{1.45}Nd_{0.40}Yb_{0.15}PDC_3(H_2O)_3]\cdot H_2O$ (~0.068 *K*), La_2O_3: Yb^{3+}/Nd^{3+} (~0.1 *K*), $LaPO_4$: Yb^{3+}/Nd^{3+} (~0.02 *K*) and Ag/Ag_2S (~0.2 *K*) [5,20,35,38–40]. On the basis of the above discussion, the optical thermometry realized by the thermally enhanced NIR to NIR PL in NLYN@SiO_2@Cu_2S NCs reveals ultrahigh sensitivity and resolution, which can be expected to be used for biomedicine.

3.4. Photothermal conversion effect

In order to evaluate the photothermal conversion performance of the prepared samples driven by NIR light, the temperature variations of NLYN, NLYN@SiO_2 and NLYN@SiO_2@Cu_2S NCs dispersed in PBS solution (1 mg/mL) are monitored by a thermocouple thermometer as a function of 980 nm-excited time and power density respectively, as illustrated in Fig. 9(a)–(c). Notably, the temperature of Cu_2S-adhered NCs is quickly increased from room temperature to equilibrium point 318.6 *K* (45.6 °C) under the continuous 980 nm irradiation (7.04 mW/mm^2) of about 180 s, from which a large temperature increment of about 20 *K* is obtained. However, the magnitude of temperature change in NLYN (2.9 *K*) and NLYN@SiO_2 (3.8 *K*) NCs is insignificant, demonstrating that the remarkable light-to-heat conversion capacity of NLYN@SiO_2@Cu_2S NCs derives from the modification of small Cu_2S NCs, which possess outstanding absorption and conversion ability for NIR light. Meanwhile, the power density dependent temperature rising properties of NLYN@SiO_2@Cu_2S NCs are also investigated with a fixed radiation time of 180 s. As plotted in Fig. 9(c), the sample temperature increases almost linearly with the elevated irradiation intensity and reaches about 340 *K* (67 °C) at 13.3 mW/mm^2, which is high enough to kill the cancer cells in biological tissues. In addition, it can be seen from Fig. 9(c) that the highest temperature of the NCs can be simply adjusted by varying the radiation intensity of NIR light to not only treat the tumors effectively but also avoid to damage the normal cells caused by overheating effect.

Generally speaking, the *E. coli* can be eliminated when the environment temperature exceeds 45 °C [41]. Coincidently, this temperature condition can be realized by the NIR-driven NLYN@SiO_2@Cu_2S NCs, referring to the above description. Therefore, a bactericidal experiment based on *E. coli* is designed to ulteriorly assess the photothermal conversion capability of Cu_2S-modified NCs. In this experiment, four groups of colonies with almost the same amount of *E. coli* are incubated in the PBS buffer solution, named as Group control, Group NIR, Group NCs and Group NCs+NIR, respectively. Among them, the *E. coli* in Group NCs and Group NCs+NIR are all cultured with the same amount of NLYN@SiO_2@Cu_2S NCs. Meanwhile, Group NIR and Group NCs+NIR are irradiated by the 980 nm NIR light with a power density of 12 mW/mm^2 for 15 min. After that, the four bacterial groups are all cultivated at 37 °C for 24 h in the air and then taken out to observe the bacterial amount of each group. As visualized in Fig. 9(d), the numbers of surviving bacteria in Group NIR and Group NCs are similar as that of Group control, indicating that it is ineffective to kill the *E. coli* only by the irradiation of 980 nm NIR light or the NLYN@SiO_2@Cu_2S NCs. By contrast, most of the bacteria in Group NCs+NIR are eliminated by the high temperature, originating from the excellent light-to-heat conversion ability of the presented NCs driven by NIR light.

Table 1
Various Nd^{3+}-based optical thermometers with relevant parameters.

Material	Dopant	EX	TCLs	Wavelength (nm)	T (*K*)	ΔE (cm^{-1})	S_R (K^{-1})	S_A (% K^{-1})	Ref.
NLYN@SiO_2@Cu_2S	Yb^{3+}/Nd^{3+}	980 nm	$^4F_{7/2}$, $^4F_{5/2}$	700–900	298–573	965	1388/T^2	0.11	This work
			$^4F_{5/2}$, $^4F_{3/2}$	700–900	298–573	1042	1498/T^2	37.8	This work
			$^4F_{7/2}$, $^4F_{3/2}$	700–900	298–573	2125	3055/T^2	19.6	This work
$LaPO_4$	Yb^{3+}/Nd^{3+}	980 nm	$^4F_{7/2}$, $^4F_{5/2}$	700–900	280–490	943	1356/T^2	0.11	[5]
			$^4F_{5/2}$, $^4F_{3/2}$	700–900	280–490	938	1348/T^2	18.53	[5]
			$^4F_{7/2}$, $^4F_{3/2}$	700–900	280–490	1914	2752/T^2	7.36	[5]
$CaWO_4$	$Yb^{3+}/Nd^{3+}/Li^+$	980 nm	$^4F_{7/2}$, $^4F_{5/2}$	700–950	303–773	817	1174/T^2	0.1	[15]
			$^4F_{5/2}$, $^4F_{3/2}$	700–950	303–773	846	1216/T^2	0.39	[15]
			$^4F_{7/2}$, $^4F_{3/2}$	700–950	303–773	1654	2377/T^2	0.36	[15]
$NaYF_4$	Yb^{3+}/Nd^{3+}	980 nm	$^4F_{7/2}$, $^4F_{5/2}$	720–950	297–400	896	1288/T^2	–	[19]
			$^4F_{5/2}$, $^4F_{3/2}$	720–950	297–400	719	1033/T^2	–	[19]
			$^4F_{7/2}$, $^4F_{3/2}$	720–950	297–400	1444	2076/T^2	–	[19]
$Ba_4La_2Ti_4Nb_6O_{30}$	Yb^{3+}/Nd^{3+}	980 nm	$^4F_{7/2}$, $^4F_{5/2}$	700–950	303–573	795	1143/T^2	0.08	[34]
			$^4F_{5/2}$, $^4F_{3/2}$	700–950	303–573	1087	1563/T^2	3.1	[34]
			$^4F_{7/2}$, $^4F_{3/2}$	700–950	303–573	1882	2706/T^2	1.3	[34]
La_2O_3	Yb^{3+}/Nd^{3+}	980 nm	$^4F_{7/2}$, $^4F_{5/2}$	725–850	293–1233	928	1334/T^2	0.03	[35]
Glass ceramic	Yb^{3+}/Nd^{3+}	980 nm	$^4F_{7/2}$, $^4F_{5/2}$	720–900	303–623	1226	1763/T^2	0.07	[36]
			$^4F_{5/2}$,$^4F_{3/2}$	720–900	303–623	1311	1884/T^2	2.7	[36]
			$^4F_{7/2}$, $^4F_{3/2}$	720–900	303–623	2094	3010/T^2	0.9	[36]

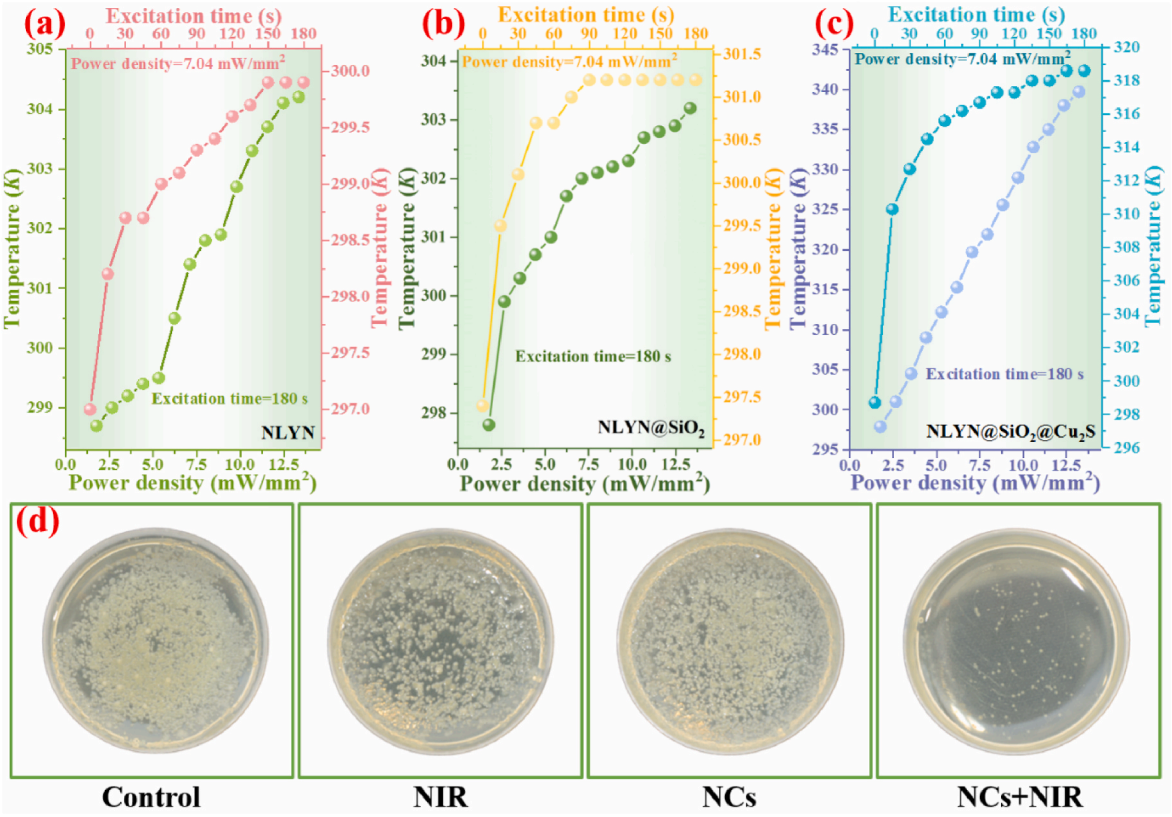

Fig. 9. The photothermal conversion effect of (a) NLYN NCs, (b) NLYN@SiO_2 NCs and (c) NLYN@SiO_2@Cu_2S NCs radiated by 980 nm wavelength. (d) Digital photo of *E. coli* incubated under various conditions.

4. Conclusions

In summary, thermal-enhanced NIR to NIR luminescence is obtained in NLYN@SiO_2@Cu_2S NCs, by which the outstanding temperature sensing behaviors operating in the biological window are realized with ultrahigh thermal sensitivity ($S_{A\text{-}Max} = 37.8\%\ K^{-1}$, $S_{R\text{-}Max} = 3.45\%\ K^{-1}$) and resolution (below 0.08 *K*, $\delta T_{min} = 0.009\ K$). The NIR emission of Nd^{3+}: ^4F_j (j = 7/2, 5/2, 3/2) → $^4I_{9/2}$ transition driven by 980 nm wavelength can still be captured under 8 mm tissue thickness. More importantly, the Cu_2S-modified NCs show excellent photothermal conversion capacity with the irradiation of NIR light, further demonstrated by a bactericidal experiment based on *E. coli*. The temperature around the sample can be elevated to 318.6 *K* (45.6 °C) under 180 s' NIR irradiation with a fixed power density of 7.04 mW/mm², and the final temperature can be linearly adjusted through changing the excitation power density to meet the actual requirements of PTT. The superior photothermal conversion performance combined with self-monitored temperature sensing ability based on thermal-enhanced NIR to NIR emission makes NLYN@SiO_2@Cu_2S NCs a potent competitor for PTT application.

Declaration of competing interest

The authors declare that they have no known competing financial interests or personal relationships that could have appeared to influence the work reported in this paper.

Acknowledgements

This work is financially supported by National Natural Science Foundation of China (11704054, 11874055, 12004062, 52104392), Natural Science Foundation of Chongqing (CSTB2022NSCQ-MSX0366, csct2021jcyj-msxmX0578) and Science and Technology Research Program of Chongqing Municipal Education Commission (KJZD-M202000601, KJQN202100615, KJQN202100639).

Appendix A. Supplementary data

Supplementary data to this article can be found online at https://doi.org/10.1016/j.ceramint.2023.04.037.

References

[1] Y. Xia, X. Ma, J. Gao, G. Chen, Z. Li, X. Wu, Z. Yu, J. Xing, L. Sun, H. Ruan, L. Luo, L. Xiang, C. Dong, W. Ren, Z. Shen, A. Wu, A flexible caterpillar-like gold nanoparticle assemblies with ultrasmall nanogaps for enhanced dual-modal imaging and photothermal therapy, Small 14 (2018), 1800094, https://doi.org/10.1002/smll.201800094.

[2] W. Gao, Y. Sun, M. Cai, Y. Zhao, W. Cao, Z. Liu, G. Cui, B. Tang, Copper sulfide nanoparticles as a photothermal switch for TRPV1 signaling to attenuate atherosclerosis, Nat. Commun. 9 (2018) 231, https://doi.org/10.1038/s41467-017-02657-z.

[3] L. Wen, L. Chen, S. Zheng, J. Zeng, G. Duan, Y. Wang, G. Wang, Z. Chai, Z. Li, M. Gao, Ultrasmall biocompatible WO_{3-x} nanodots for multi-modality imaging and combined therapy of cancers, Adv. Mater. 28 (2016) 5072–5079, https://doi.org/10.1002/adma.201506428.

[4] M. Hashemi, M. Omidi, B. Muralidharan, H.A. Smyth, M. Mohaheghi, J. Mohammadi, E.T. Milner, Evaluation of the photothermal properties of a reduced graphene oxide/arginine nanostructure for near-infrared absorption, ACS Appl. Mater. Interfaces 9 (2017) 32607–32620, https://doi.org/10.1021/acsami.7b11291.

[5] H. Suo, X. Zhao, Z. Zhang, C. Guo, Ultra-sensitive optical nano-thermometer $LaPO_4$: Yb^{3+}/Nd^{3+} based on thermo-enhanced NIR-to-NIR emissions, Chem. Eng. J. 389 (2020), 124506, https://doi.org/10.1016/j.cej.2020.124506.

[6] H. Suo, X. Zhao, Z. Zhang, Y. Wu, C. Guo, Up-converting $LuVO_4$: Nd^{3+}/Yb^{3+}/Er^{3+}@SiO_2@Cu_2S hollow nanoplatforms for self-monitored photothermal ablation, ACS Appl. Mater. Interfaces 10 (2018) 39912–39920, https://doi.org/10.1021/acsami.8b18184.

[7] G. Xiang, Q. Xia, X. Liu, Y. Wang, J. Sha, L. Li, X. Zhou, L. Ma, X. Wang, J. Zhang, Upconversion nanoparticles modified by Cu_2S for photothermal therapy along with

real-time optical thermometry, Nanoscale 13 (2021) 7161–7168, https://doi.org/10.1039/D0NR09115D.
[8] D. Jaque, L.M. Maestro, B.D. Rosal, P. Haro-Gonzalez, A. Benayas, J.L. Plaza, E. M. Rodriguez, J.G. Sole, Nanoparticles for photothermal therapies, Nanoscale 6 (2014) 9494–9530, https://doi.org/10.1039/C4NR00708E.
[9] J. Liu, M. Han, R. Wang, S. Xu, X. Wang, Photothermal phenomenon: extended ideas for thermophysical properties characterization, J. Appl. Phys. 131 (2022), 065107, https://doi.org/10.1063/5.0082014.
[10] H. Liang, K. Yang, Y. Yang, Z. Hong, S. Li, Q. Chen, J. Li, X. Song, H. Yang, A lanthanide upconversion nanothermometer for precise temperature mapping on immune cell membrane, Nano Lett. 22 (2022) 9045–9053, https://doi.org/10.1021/acs.nanolett.2c03392.
[11] Y. Xing, L. Li, X. Ai, L. Fu, Polyaniline-coated upconversion nanoparticles with upconverting luminescent and photothermal conversion properties for photothermal cancer therapy, Int. J. Nanomed. 11 (2016) 4327, https://doi.org/10.2147/IJN.S97441.
[12] D. Stdab, X. Yao, W. Xi, B. Artur, R. Wei, S. Lining, Nd^{3+}-sensitized upconversion nanoparticle coated with antimony shell for bioimaging and photothermal therapy invitro using single laser irradiation-ScienceDirect, J. Rare Earths 40 (2021) 862–869, https://doi.org/10.1016/j.jre.2021.05.015.
[13] P. Rodríguez-Sevilla, Y. Zhang, P. Haro-González, F. Sanz-Rodriguez, F. Jaque, J. G. Sole, X. Liu, D. Jaque, Thermal scanning at the cellular level by an optically trapped upconverting fluorescent particle, Adv. Mater. 28 (2016) 2421–2426, https://doi.org/10.1002/adma.201505020.
[14] P. Du, Q. Zhang, X. Wang, L. Luo, W. Li, Upconversion luminescence, temperature sensing and internal heating behaviors of $Er^{3+}/Yb^{3+}/Fe^{3+}$-tridoped $NaBiF_4$ nanoparticles, J. Alloys Compd. 805 (2019) 171–179, https://doi.org/10.1016/j.jallcom.2019.07.054.
[15] W. Xu, Y. Hu, L. Zheng, Z. Zhang, W. Cao, H. Liu, X. Wu, Enhanced NIR-NIR luminescence from $CaWO_4$: Nd^{3+}/Yb^{3+} phosphors by Li^+ codoping for thermometry and optical heating, J. Lumin. 208 (2019) 415–423, https://doi.org/10.1016/j.jlumin.2019.01.005.
[16] Y. Tang, W. Di, X. Zhai, R. Yang, W. Qin, NIR-responsive photocatalytic activity and mechanism of $NaYF_4$: Yb, Tm@TiO_2 core–shell nanoparticles, ACS Catal. 3 (2013) 405–412, https://doi.org/10.1021/cs300808r.
[17] Y. Dwivedi, S.C. Zilio, Infrared cascade and cooperative multicolor upconversion emissions in $Y_8V_2O_{17}$: Eu: Yb nanophosphors, Opt Express 21 (2013) 4717–4727, https://doi.org/10.1364/OE.21.004717.
[18] Y. Dwivedi, S.N. Thakur, S.B. Rai, Study of frequency upconversion in Yb^{3+}/Eu^{3+} by cooperative energy transfer in oxyfluoroborate glass matrix, Appl. Phys. B 89 (2007) 45–51, https://doi.org/10.1007/s00340-007-2747-y.
[19] W. Xu, H. Qi, L. Zheng, Z. Zhang, W. Cao, Multifunctional nanoparticles based on the Nd^{3+}/Yb^{3+} codoped $NaYF_4$, Opt. Lett. 40 (2015) 5678–5681, https://doi.org/10.1364/OL.40.005678.
[20] X. Zhou, Y. Wang, H. Wang, L. Xiang, Y. Yan, L. Li, G. Xiang, Y. Li, X. Tang, X. Zhou, Nd^{3+} and Nd^{3+}/Yb^{3+}-incorporated complexes as optical thermometer working in the second biological window, Sensing and Bio-Sensing Research 29 (2020), 100345, https://doi.org/10.1016/j.sbsr.2020.100345.
[21] Y. Zhang, H. Suo, X. Zhao, D. Sun, L. Fan, C. Cuo, NIR-to-NIR deep penetrating nanoplatforms Y_2O_3:Nd^{3+}/Yb^{3+}@SiO_2@Cu_2S towards highly efficient photothermal ablation, ACS Appl. Mater. Interfaces 10 (2018) 14570–14576, https://doi.org/10.1021/acsami.8b03239.
[22] X. Jiang, Y. Sun, X. Wang, L. Hu, S. Chen, Q. Yang, Temperature dependence of spectroscopic properties and energy transfer in Nd^{3+}/Yb^{3+} co-doped silicate glass, J. Lumin. 251 (2022), 119146, https://doi.org/10.1016/j.jlumin.2022.119146.
[23] Y. Zhang, P. Wang, H. Wang, X. Zheng, Y. Guo, N. Zhang, H. Liu, Visible and near-infrared luminescence properties of Nd^{3+}/Yb^{3+} co-doped Gd_2O_3 phosphors for highly sensitive optical thermometry, Dalton Trans. 51 (2022) 10612–10622, https://doi.org/10.1039/D2DT01271E.
[24] B.S. Richards, A. Shalav, Enhancing the near-infrared spectral response of silicon optoelectronic devices via up-conversion, IEEE Trans. Electron. Dev. 54 (2007) 2679–2684, https://doi.org/10.1109/TED.2007.903197.
[25] G. Xiang, X. Liu, J. Zhang, Z. Liu, W. Liu, Y. Ma, S. Jiang, X. Tang, X. Zhou, L. Li, Y. Jin, Dual-mode optical thermometry based on the fluorescence intensity ratio excited by a 915 nm wavelength in $LuVO_4$: Yb^{3+}/Er^{3+}@SiO_2 nanoparticles, Inorg. Chem. 58 (2019) 8245–8252, https://doi.org/10.1021/acs.inorgchem.9b01229.
[26] M.K. Mahata, T. Koppe, T. Mondal, C. Brusewitz, K. Kumar, V.K. Rai, H. Hofsass, U. Vetter, Incorporation of Zn^{2+} ions into $BaTiO_3$:Er^{3+}/Yb^{3+} nanophosphor: an effective way to enhance upconversion, defect luminescence and temperature sensing, Phys. Chem. Chem. Phys. 17 (2015), 20741, https://doi.org/10.1039/C5CP01874A.
[27] S. Sinha, M.K. Mahata, K. Kumar, Enhancing the upconversion luminescence properties of Er^{3+}–Yb^{3+} doped yttrium molybdate through Mg^{2+} incorporation: effect of laser excitation power on temperature sensing and heat generation, New J. Chem. 43 (2019) 5960–5971, https://doi.org/10.1039/C9NJ00760A.
[28] Z.C. Wu, L.L. Cui, X. Zhang, X.X. Zhang, J. Liu, L. Ma, X.J. Wang, J.L. Zhang, Cationic substitution induced tuning of photoluminescence in $Ba_{2.\ 94-2x}La_xNa_xP_4O_{13}$: 0.06 Eu phosphors for WLEDs, J. Alloys Compd. 835 (2020), 155109, https://doi.org/10.1016/j.jallcom.2020.155109.
[29] G. Xiang, J. Zhang, Z. Hao, X. Zhang, Y. Luo, S. Lu, H. Zhao, Transition to cubic phase and enhancement of green upconversion emission by adding La^{3+} ions in hexagonal $NaLuF_4$: Yb^{3+}/Er^{3+} nanocrystals, CrystEngComm 16 (2014) 2499–2507, https://doi.org/10.1039/C3CE42490A.
[30] G. Xiang, J. Zhang, Z. Hao, X. Zhang, G.H. Pan, Y. Luo, W. Lu, H. Zhao, Importance of suppression of Yb^{3+} de-excitation to upconversion enhancement in β-$NaYF_4$: Yb^{3+}/Er^{3+}@β-$NaYF_4$ sandwiched structure nanocrystals, Inorg. Chem. 54 (2015) 3921–3928, https://doi.org/10.1021/acs.inorgchem.5b00109.
[31] P. Du, L. Luo, Q. Yue, W. Li, The simultaneous realization of high- and low-temperature thermometry in Er^{3+}/Yb^{3+}-codoped Y_2O_3 nanoparticles, Mater. Lett. 143 (2015) 209–211, https://doi.org/10.1016/j.matlet.2014.12.123.
[32] X. Tian, X. Wei, Y. Chen, C. Duan, M. Yin, Temperature sensor based on ladder-level assisted thermal coupling and thermal-enhanced luminescence in $NaYF_4$: Nd^{3+}, Opt Express 22 (2014) 30333–30345, https://doi.org/10.1364/OE.22.030333.
[33] B. Kateb, V. Yamamoto, C. Yu, W. Grundfest, J.P. Gruen, Infrared thermal imaging: a review of the literature and case report, Neuroimage 47 (2009) T154–T162, https://doi.org/10.1016/j.neuroimage.2009.03.043.
[34] Y. Shi, F. Yang, C. Zhao, Y. Huang, M. Li, Q. Zhou, Q. Li, Z. Li, J. Liu, T. Wei, Highly sensitive up-conversion thermometric performance in Nd^{3+} and Yb^{3+} sensitized $Ba_4La_2Ti_4Nb_6O_{30}$ based on near-infrared emissions, J. Phys. Chem. Solid. 124 (2019) 130–136, https://doi.org/10.1016/j.jpcs.2018.09.013.
[35] G. Gao, D. Busko, S. Kauffmann-Weiss, A. Turshatov, I.A. Howard, B.S. Richards, Wide-range non-contact fluorescence intensity ratio thermometer based on Yb^{3+}/Nd^{3+} co-doped La_2O_3 microcrystals operating from 290 to 1230 K, J. Mater. Chem. C 6 (2018) 4163–4170, https://doi.org/10.1039/C8TC00782A.
[36] W. Xu, H. Zhao, Z. Zhang, W. Cao, Highly sensitive optical thermometry through thermally enhanced near infrared emissions from Nd^{3+}/Yb^{3+} codoped oxyfluoride glass ceramic, Sensor. Actuator. B Chem. 178 (2013) 520–524, https://doi.org/10.1016/j.snb.2012.12.050.
[37] Y. Wu, H. Suo, D. He, C. Guo, Highly sensitive up-conversion optical thermometry based on Yb^{3+}-Er^{3+} co-doped $NaLa(MoO_4)_2$ green phosphors, Mater. Res. Bull. 106 (2018) 14–18, https://doi.org/10.1016/j.materresbull.2018.05.019.
[38] H. Zhang, J. Ye, X. Wang, S. Zhao, R. Lei, L. Huang, S. Xu, Highly reliable all-fiber temperature sensor based on the fluorescence intensity ratio (FIR) technique in Er^{3+}/Yb^{3+} co-doped $NaYF_4$ phosphors, J. Mater. Chem. C 7 (2019) 15269–15275, https://doi.org/10.1039/c9tc05011f.
[39] E. Casagrande, M. Back, D. Cristofori, J. Ueda, S. Tanabe, S. Palazzolo, F. Rizzolio, V. Canzonieri, E. Trave, P. Riello, Upconversion-mediated Boltzmann thermometry in double-layered Bi_2SiO_5: Yb^{3+}, Tm^{3+}@SiO_2 hollow nanoparticles, J. Mater. Chem. C 8 (2020) 7828–7836, https://doi.org/10.1039/x0xx00000x.
[40] D. Ruiz, B.D. Rosal, M. Acebron, C. Palencia, C. Sun, J. Cabanillas-Gonzalez, M. Lopez-Haro, A.B. Hungria, D. Jaque, B.H. Juarez, Ag/Ag_2S nanocrystals for high sensitivity near-infrared luminescence nanothermometry, Adv. Funct. Mater. 27 (2017), 1604629, https://doi.org/10.1002/adfm.201604629.
[41] F. Annesi, A. Pane, M.A. Losso, A. Guglielmelli, F. Lucente, F. Petronella, T. Placido, R. Comparelli, M.G. Guzzo, M.L. Curri, R. Bartolino, L.D. Sio, Thermo-plasmonic killing of Escherichia coli TG1 bacteria, Materials 12 (2019) 1530, https://doi.org/10.3390/ma12091530.